J. Phys. Chem. A **2005,** *109,* 8507−8514

Asymmetric Top Rotors in Electric Fields: Influence of Chaos and Collisions in Molecular Beam Deflection Experiments

M. Abd El Rahim, R. Antoine,* M. Broyer, D. Rayane, and Ph. Dugourd

Laboratoire de Spectrométrie Ionique et Moléculaire, UMR 5579 (Université Lyon I et CNRS),
43 Bd du 11 Novembre 1918, 69622 Villeurbanne cedex, France

Received: June 10, 2005; In Final Form: July 21, 2005

We report on electric deflection experiments of structural isomers of aminobenzonitrile. They are used as models to study the influence of the asymmetry of a molecule on the molecule−electric field interaction. Experimental deflection profiles are compared to Stark effect calculations. We found increasing deviations from the calculated Stark effect behavior with increasing asymmetry. This deviation is induced by interactions with other particles and is directly related to the chaotic behavior of the rotational motion of asymmetric rotors in a static electric field.

1. Introduction

Over the past decade, a large effort has been devoted to manipulating molecules, in particular, to study the influence of their orientation in chemical processes.[1] While the most common way is the use of intense laser fields, orientation and deceleration of polar molecules can also be obtained using electrostatic devices such as hexapoles[2−4] or strong electric fields.[5−7] Besides reactive scattering studies, these electrostatic methods have found numerous applications in spectroscopic, cooling, and photodissociation experiments.[1] These techniques have mainly been used for the first rotational states of small rigid rotors. Inhomogeneous electric fields can also be used to deflect molecular beams and to measure permanent or induced dipoles of isolated molecules.[8,9] In this case, results are available for a large variety of systems ranging from atoms and diatomic molecules[10] to clusters and polypeptides.[11−13]

For a symmetric toplike rigid rotor, the deflection of the molecule is due to first-order Stark effect and is deduced from the calculation of the energy of the rotational levels of the molecule in the electric field. The electric field induces a dispersion of the molecular beam. In the general case, however, the simple approach used for rigid rotors in a static electric field is no longer valid.[14,15] In the limiting case of molecules with strong couplings between rotation and vibration, a statistical orientation of the molecules in the electric field, similar to paraelectricity, is observed. In particular, this statistical orientation was observed for hot molecules[16,17] and for flexible systems.[13,18] In this case, all the molecules are deflected by the same amount. The average dipole does not depend on the initial rotation of the molecule and is described by the Debye linear response theory.[19,20] While the linear response theory provides an easy way of understanding the data, a detailed justification of its validity for molecules in the gas phase and an understanding of the transition from the broadening observed for rigid symmetric rotors to the global deflection predicted by the linear response are not yet available.

Between rigid symmetric rotors (where K and M are good rotational quantum numbers) and large systems (where rotation and vibration Hamiltonians cannot be separated), asymmetric top molecules in electric fields (with the loss of K as a good rotational quantum number) appear as intermediates. In this paper, we present electric deflections of disubstituted benzene derivative molecules. We chose the structural isomers of aminobenzonitrile (ABN) molecules. These molecules have strong permanent dipole moments. By varying the position of substituents, from para to ortho, the asymmetry of the molecule can be changed. Thus, they represent models to study the influence of the asymmetry of a molecule in electric deflection experiments.

2. Experimental Section

The experimental apparatus consists of a molecular beam source coupled to an electric deflector and a time-of-flight mass spectrometer. The molecular beam is produced by a laser vaporization source. *Para*-aminobenzonitrile (PABN), *meta*-aminobenzonitrile (MABN), and *ortho*-aminobenzonitrile (OABN) are purchased from Sigma (purity ≥ 98%). For MABN and OABN, the sample is mixed with cellulose in a 1:3 ratio, whereas for PABN, we used a 1:10 ratio. The mixing is pressed under 10^4 bars in a cylindrical mold to form a solid rod. The third harmonic of a Nd^{3+}:YAG laser is used for the ablation of the rod that is rotated and translated in a screw motion. A short pulse of helium, synchronized with the ablation laser, is supplied by a piezo valve. A constant leak of carrier gas could be added to the helium pulse by applying a small additional constant voltage to the piezo valve. At the exit of the source, the molecules are thermalized in a 5-cm-long and 3-mm-diameter chamber maintained at room temperature. A thermal molecular beam is produced without supersonic expansion. Note that no alignment of the molecules in the beam is observed as can be observed in supersonic beams.[21] After two skimmers (1.5-mm and 2-mm diameters), the beam is collimated by two rectangular slits (∼0.35-mm width and separated by 0.6 m). The beam velocity is selected and measured with a mechanical chopper located in front of the first slit. Then, the beam travels through a 15-cm-long electric deflector. The geometry provides an inhomogeneous electric field which is equivalent to an “electrical two-wire field”. The electric field F and its gradient ∇F are perpendicular to the beam axis and are nearly constant over its width. For a voltage of 20 kV, the electric field and the gradient

---

* Corresponding author: rantoine@lasim.univ-lyon1.fr.

10.1021/jp053127p CCC: $30.25 © 2005 American Chemical Society
Published on Web 09/03/2005

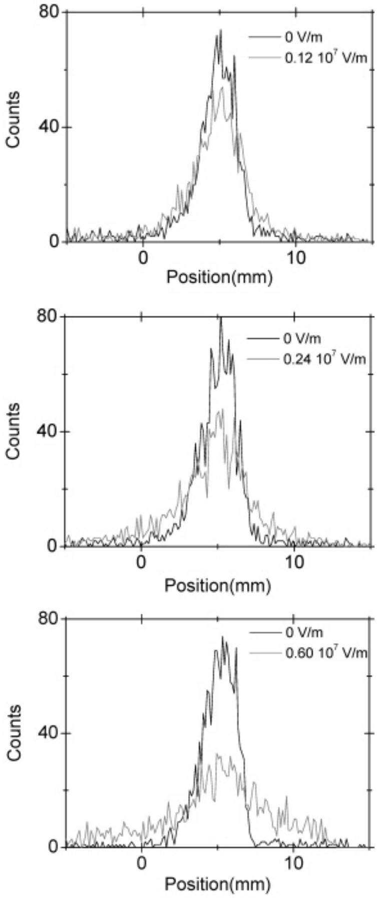

Figure 1. Experimental beam profiles of PABN obtained at different electric fields across the deflector. The electric field values are given in the figure.

of the electric field in the deflector are $F = 1.21\ 10^7$ V/m and $\nabla F = 2.09\ 10^9$ V/m^2.

Beam profiles are analyzed 1.025 m after the deflector, with a time-of-flight mass spectrometer coupled to a position-sensitive detector. The neutral particles from the beam are ionized by the fourth harmonics of a Nd^{3+}: YAG laser (266 nm) in the extraction region of the linear time-of-flight mass spectrometer. The mass spectrometer consists of an extraction region, an acceleration region, two deflection electrodes, an electrostatic lens, and a free-flight region. The electrostatic lens, located ~30 cm after the extraction region, has been specially designed to magnify the ion image on the axis of the electric deflection. The detector is located 1 m after the acceleration plate. It is a pair of microchannel plates coupled to two orthogonal delay lines. The time-of-flight, the detector, its electronics, and the data processing are discussed in ref 22. The arrival time at the detector and the position on the detector are recorded for each ion. Data are recorded as a function of the electric field in the deflector.

3. Experimental Results

Figure 1 displays the experimental beam profiles (projection of the images on the axis of the electric field in the deflector) of PABN molecules recorded without and at different voltages across the electric deflector. The experimental profiles that are obtained with an electric field are symmetrically broadened. This broadening increases as the electric field in the deflector increases. Profiles were systematically recorded as a function of the electric field inside the deflector from 0 V/m to $1.21\ 10^7$ V/m. In Figure 2, we have plotted the variation in the intensity of the signal at the maximum of the peak (I/I_0) as a function of the electric field F for PABN, MABN, and OABN molecules. A regular decrease in the signal is observed as F increases. This diminution in the intensity at the maximum reflects the increase in the broadening due to the interaction with the electric field. To reproduce these curves, we have to simulate the rotation of the polar asymmetric molecule in a static electric field. For that, we need the rotational constants and dipole moment components of the three molecules. This calculation is described in section 4. Then, we need to simulate the Stark effect for an asymmetric top rotor. The quantum mechanical approach that we used is described in section 5.

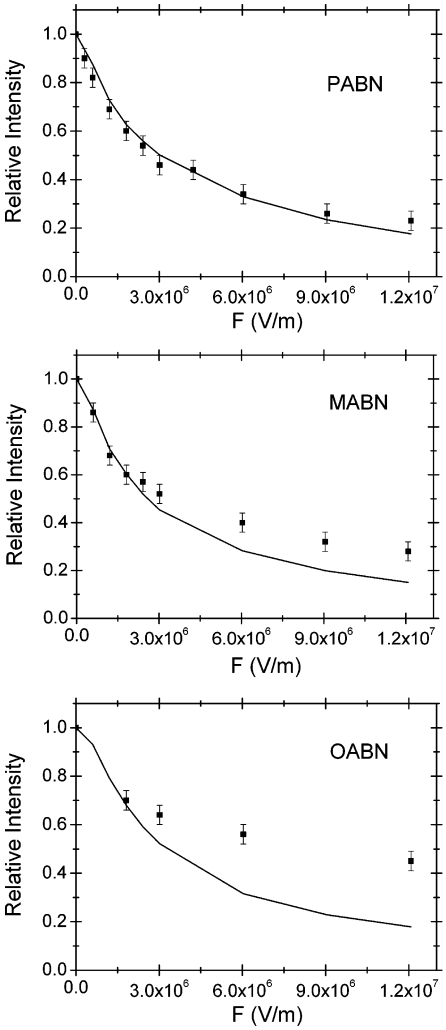

Figure 2. Relative intensity of the beam profile on the beam axis as a function of the electric field F. Squares correspond to experimental data and the lines to the quantum simulations performed using dipole values and rotational constants given by MP2 calculations (see Table 1).

4. Geometry Optimizations and Calculated Dipole Moments of the Structural Isomers of Aminobenzonitrile Molecules

During a previous study on the *para*-aminobenzoic acid, we showed that density functional theory (DFT) calculations significantly overestimate the value of the permanent electric dipole, whereas Hartree−Fock with second-order Møller−Plesset corrections (MP2) calculations seemed to be an accurate approach for such molecules with large internal charge transfer.[23] This trend was recently confirmed.[24] All the calculations were

TABLE 1: Energies, Rotational Constants, and Calculated Electric Dipole Components of PABN, MABN, and OABN Obtained at MP2 Level of Theory

	basis set	energy (hartree)	rotational constants (cm^{-1})			dipole components (debye)			
			A	B	C	μ_a	μ_b	μ_c	μ total
PABN									
MP2	6-311++G**	-378.8568	0.18549	0.03270	0.02782	5.94	0.00	1.03	6.03
expt[a]			0.18610(2)	0.033032(6)	0.028066(6)	6.41(3)			
MABN									
MP2	6-311++G**	-378.8561	0.1116	0.0400	0.02947	-5.17	0.51	1.08	5.29
OABN									
MP2	6-311++G**	-378.8584	0.09951	0.04989	0.03326	−3.61	1.62	0.94	4.07

[a] References 26, 35.

performed with *Gaussian 98*,[25] with the basis set 6-311++G**. A full geometry optimization was performed at the MP2 level of theory. Results are presented in Table 1, and the lowest-energy structures for aminobenzonitrile isomers are displayed in Figure 3. For PABN, the phenyl ring and the nitrile function are in the same plane; the NH_2 group is out of plane. This nonplanar geometry gives rise to a non-null value of the dipole moment along the *c*-axis (see Figure 3). For MABN and OABN, the NH_2 group is also found out of the plane of the benzyl ring, and the molecule has a non-null value of the dipole moment along the *c*-axis. In addition, there is a non-null value of the dipole moment along the *b*-axis. The calculation for PABN can be compared to experimental results obtained by Stark effect studies of rotationally resolved electronic spectra.[26] An acceptable agreement between experiment and MP2 results is observed for both rotational constants and dipole moment components. MP2 values can also be compared to the values obtained from the additivity of bond dipole moments, i.e., $\vec{\mu}_{\mathrm{ABN}} = \vec{\mu}_{\mathrm{AN}} + \vec{\mu}_{\mathrm{BN}}$ (where $\vec{\mu}_{\mathrm{AN}}$ is the dipole of aniline (1.13 D) and $\vec{\mu}_{\mathrm{BN}}$ is the dipole of benzonitrile (4.48 D)). This crude method gives, respectively, 5.61, 5.13, and 4.03 D for PABN, MABN, and OABN. These values are relatively close to MP2 values.

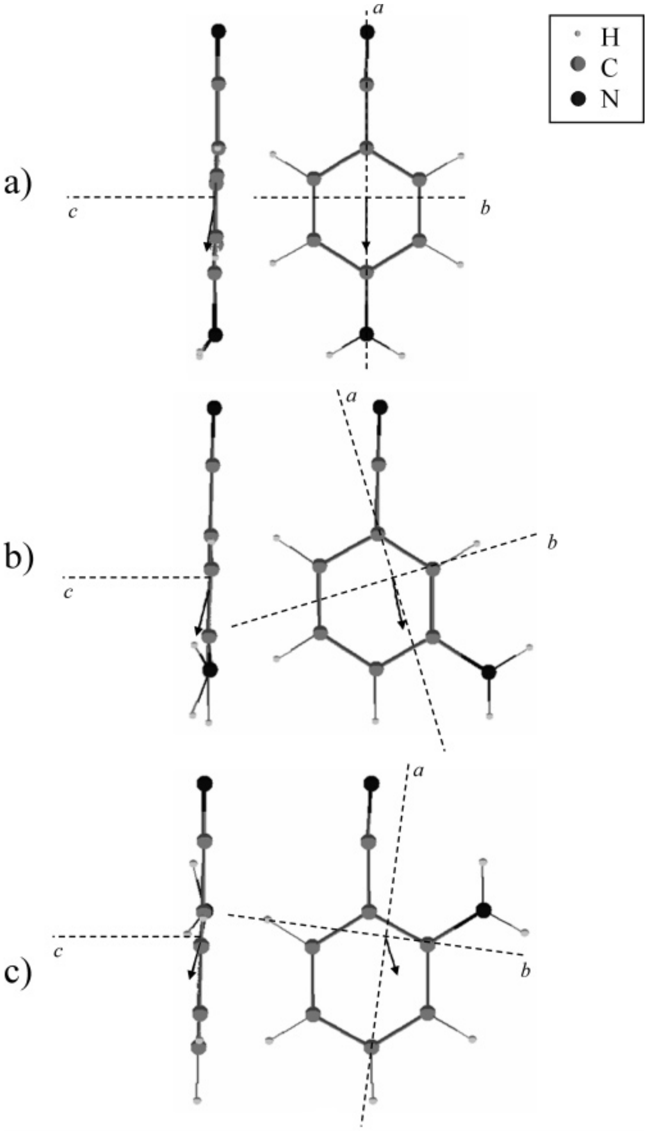

Figure 3. Geometry of the lowest-energy conformation found at the MP2 6−311++G** level of theory for (a) PABN, (b) MABN, and (c) OABN molecules (chemical formula $H_2N-C_6H_4-CN$). The arrows show the direction and the relative magnitude of the electric dipole moment. The dashed lines display the direction of the principal axes of inertia.

Finally, from the rotational constants ($A > B > C$), one can define an asymmetric parameter given by

$$\kappa = \frac{2B - A - C}{A - C} \tag{1}$$

This parameter varies from −1 (prolate symmetric top, $B = C$) to +1 (oblate symmetric top, $A = B$). It is equal to −0.938 for PABN, −0.744 for MABN, and −0.498 for OABN. Thus, PABN is a symmetric toplike prolate molecule, OABN is strongly asymmetric, and MABN is an intermediate case.

5. Calculation of Rotational Energies and Deflection Profiles

5.1. Calculation of Stark Asymmetric Rotor Energies. The Hamiltonian for an asymmetric rigid rotor in an electric field may be written

$$H = H_{\mathrm{rot}} + H_{\mathrm{Stark}} \tag{2}$$

$$H_{\mathrm{rot}} = AJ_a^{\ 2} + BJ_b^{\ 2} + CJ_c^{\ 2} \tag{3}$$

where *a*, *b*, and *c* are the principal axis of inertia of the rotor; J_a, J_b, and J_c are the corresponding components of the angular momentum, and *A*, *B*, and *C* are the rotational constants (in cm^{-1}; $A > B > C$).

The Stark contribution to the Hamiltonian may be written

$$H_{\mathrm{Stark}} = -\vec{\mu}\vec{F} = -F_Z \sum_{g=a,b,c} \mu_g \phi_{Zg} \tag{4}$$

where *Z* has been chosen as the field direction in a laboratory fixed coordinate system, μ_g are the components of the dipole moment along the principal inertial axes, and ϕ_{Zg} is the direction cosine or projection of the various molecular axes onto the field direction *Z*.

The eigenvalues of the Hamiltonian *H* are obtained by numerical diagonalization of the corresponding matrix on the basis of the eigenvectors of the prolate symmetric rotor. On this basis, the matrix elements for H_{rot} may be written[27,28]

$$\langle JKM|H_{\mathrm{rot}}|JKM\rangle = \frac{B+C}{2}[J(J+1) - K^2] + AK^2 \quad (5)$$

$$\langle JKM|H_{\mathrm{rot}}|JK \pm 2M\rangle = \frac{C-B}{4}[J(J+1) - (K\pm 1)(K\pm 2)]^{1/2} \times [J(J+1) - K(K\pm 1)]^{1/2} \quad (6)$$

The matrix elements for H_{Stark} corresponding to the μ_a, μ_b, and μ_c components of the dipole are given below: Contributions of μ_a

$$\langle JKM|H_{\mathrm{Stark}}|JKM\rangle = -\frac{MK}{J(J+1)}\mu_a F_Z \quad (7)$$

$$\langle J+1KM|H_{\mathrm{Stark}}|JKM\rangle = -\frac{[(J+1)^2 - K^2]^{1/2}[(J+1)^2 - M^2]^{1/2}}{(J+1)[(2J+1)(2J+3)]^{1/2}}\mu_a F_Z \quad (8)$$

Contributions of μ_c

$$\langle JK\pm 1M|H_{\mathrm{Stark}}|JKM\rangle = -\frac{M[(J\mp K)(J\pm K+1)]^{1/2}}{2J(J+1)}\mu_c F_Z \quad (9)$$

$$\langle J+1K\pm 1M|H_{\mathrm{Stark}}|JKM\rangle = \pm\frac{[(J\pm K+1)(J\pm K+2)]^{1/2}[(J+1)^2 - M^2]^{1/2}}{2(J+1)[(2J+1)(2J+3)]^{1/2}}\mu_c F_Z \quad (10)$$

Contributions of μ_b are imaginary

$$\langle JK\pm 1M|H_{\mathrm{Stark}}|JKM\rangle = \pm i\frac{M[(J\mp K)(J\pm K+1)]^{1/2}}{2J(J+1)}\mu_b F_Z \quad (11)$$

$$\langle J+1K\pm 1M|H_{\mathrm{Stark}}|JKM\rangle = -i\frac{[(J\pm K+1)(J\pm K+2)]^{1/2}[(J+1)^2 - M^2]^{1/2}}{2(J+1)[(2J+1)(2J+3)]^{1/2}}\mu_b F_Z \quad (12)$$

If $\mu_b \neq 0$, some of the matrix elements are complex. We write the Hamiltonian as

$$H = \mathcal{A} + i\mathcal{B} \quad (13)$$

where $\mathcal{A}$ and $\mathcal{B}$ are both real matrices of dimension n. The eigenvalues of H are identical to those of the supermatrix

$$\begin{bmatrix} \mathcal{A} & -\mathcal{B} \\ \mathcal{B} & \mathcal{A} \end{bmatrix} \quad (14)$$

of dimension $2n$. This supermatrix has n eigenvalues doubly degenerate.

M is a good quantum number, and the supermatrix can be separated into independent blocks. Each block is labeled by the value of M. Before diagonalization, the matrix is truncated ($J \leq J_{\mathrm{max}}$). The eigenvalues E_i^M are then obtained by numerical diagonalization of each block (with $0 \leq i < \sum_{J=|M|}^{J_{\mathrm{Max}}}(2J+1)$).

5.2. Calculation of Electric Deflection Profiles. In the deflector, for each quantum state (M, i), the force is $f_i^M = -\nabla\vec{E}_i^M$ and can be written as

$$f_i^M = -\frac{\partial E_i^M}{\partial F_Z}\frac{\partial F_Z}{\partial Z} \quad (15)$$

The derivative of the energy as a function of the electric field is calculated numerically by $\partial E_i^M/\partial F_Z \cong \Delta E_i^M/\Delta F_Z$ with $\Delta F_Z/F_Z = 0.5\%$. Thus, the deflection for each quantum state is given by

$$d_i^M = -\frac{K_{\mathrm{g}}}{mv^2}\frac{\Delta E_i^M}{\Delta F_Z}\frac{\partial F_Z}{\partial Z} \quad (16)$$

where K_{g} is a geometrical constant, and m and v are the mass and the velocity of the molecule. To get a calculated profile of deflection, one has to take into account every rotational state with a statistical weight p_i^M related to the temperature T of the molecules. We assume that the molecules adiabatically enter the electric field.[29] In the adiabatic calculation, for a given M value, the order of energy levels does not change while the molecule enters the electric field. The population is given by

$$p_i^M = \exp\left(-\frac{E_i^M|_{F_Z=0}}{kT}\right) \quad (17)$$

To limit the number of rotational levels that need to be included in the simulation and the size of the matrix (eq 14), we performed the simulations at a temperature lower than the experimental one. The value of the electric field is changed in the same way. These changes have no effect on the calculated profiles.[30] Experiments are performed at $T_{\mathrm{exp}} = 300$ K. Calculations were performed at $T^* = T_{\mathrm{exp}}/30$ and with $F^* = F_{\mathrm{exp}}/30$. All the rotational levels with $J \leq J_{\mathrm{max}}$ ($J_{\mathrm{max}} = 35$) were included in the simulation.

For a given electric field, the simulation leads to a spectrum of lines $g(x)$ (x corresponds to the deflection and $g(x)$ to the intensity of the line). For the simulation of experimental profiles, this spectrum of lines has to be convoluted with a function which takes into account the initial profile of the molecular beam $f_{\mathrm{beam}}(x)$, the resolution of the apparatus ($f_{\mathrm{TOF}}(x)$ and $f_{\mathrm{PSD}}(x)$) and the magnifying factor G of the electrostatic lens. $f_{\mathrm{beam}}(x)$ has a trapezoidal shape (1.3 mm at the bottom and 0.35 mm at the top). $f_{\mathrm{TOF}}(x)$ and $f_{\mathrm{PSD}}(x)$ have Gaussian shapes with, respectively, 100 μm and 250 μm for the full width at half-maximum. Finally $G = -3.5$ is the experimental zoom factor of the electrostatic lens. After convolution, the profile can be compared to the experimental one.

6. Discussion

We have simulated electric deflection profiles following the procedure described in section 5 and using rotational constants and dipole moment components from MP2 calculations (see Table 1). Figure 2 shows the evolution of I/I_0 ratios calculated for PABN, MABN, and OABN molecules (solid line). A good agreement is obtained for PABN. For MABN and OABN, the simulation does not reproduce the experiment. This is particularly true for OABN, for $F > 3.0 \times 10^6$ V/m. The experimental I/I_0 ratio is higher than the calculated one.

We will show in the next paragraphs of this article that the difference observed for OABN and MABN between experiment and simulations is due to interactions with other particles and is directly related to the chaotic behavior of the rotational motion of asymmetric molecules in electric fields.[31] The amount of chaos depends on the degree of asymmetry of the molecule (determined from the rotational constants) and on the coupling with the electric field (determined from the dipole component values and the strength of the electric field).

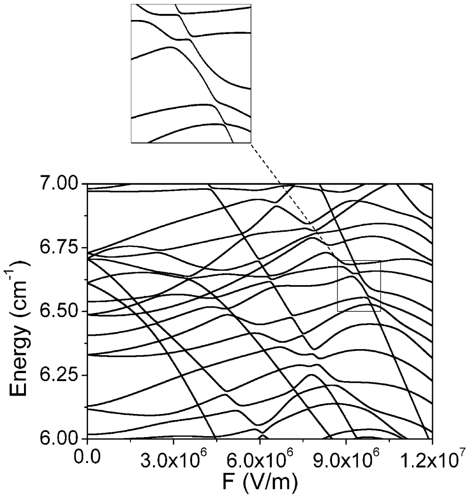

Figure 4. Electric field dependence of the 108th to the 125th energy levels for OABN molecule (for $M = 1$). The inset shows a zoom of the spectrum where avoided crossings are present.

6.1. Statistical Analysis of Rotational Spectra. Figure 4 shows the electric field dependence of the 108th to the 125th energy levels for the OABN molecule for $M = 1$. This corresponds to $8 \leq J \leq 13$. This figure illustrates the typical behavior of asymmetric top molecules in an electric field. All the crossings are avoided with different energy gaps as illustrated in the inset of the Figure 4. In Figure 4, we see that, for $F = 0$ V/m, the energy spacing between rotational lines is very irregular, and that series of levels are nearly degenerated. On the other hand, for $F = 1.2 \times 10^7$ V/m because of the repulsion between the different rotational levels, the spacing is much more regular. This sample of levels illustrates the typical pattern of spectra of classically integrable systems ($F = 0$) as opposed to nonintegrable systems ($F \neq 0$).

To quantitatively express the different character between ABN isomers, following previous works,[31,32] a statistical analysis of the rotational spectra of ABN molecules in an electric field has been performed. Figure 5 shows the nearest-neighbor spacing (NNS) histograms for the energy levels with $M = 1$ for OABN and PABN in the presence of an electric field ($F = 1.21 \times 10^7$ V/m). The procedure used to obtain these histograms is described in appendix A. The left NNSs in the figure are calculated for the 700 low-lying levels, whereas the right ones are calculated for the 700 intermediate levels (i.e., 701th to 1400th levels). We see that, for OABN, the histogram of the 700 low-lying levels is close to a Wigner distribution (dashed line in Figure 5c). This is not true for the histogram of PABN. The histograms for the 700 intermediate levels belong to an intermediate range where the coupling and the repulsion between different levels is less pronounced. In this case, the distribution of levels is more irregular than for the series of lowest energy levels. This is particularly clear for the 700 intermediate levels of PABN where a distribution close to the Poisson distribution (dashed line in Figure 5b) is observed. The difference in statistics observed between lowest energy levels and intermediate energy levels was already observed for the H_2O molecule in a strong electric field.[31] The lowest angular momentum states are more strongly perturbed by the electric field.

The histograms can be simulated by a Brody distribution, and a q parameter is defined by eq A.5 (see appendix A). q is obtained by a least-squares fit of the Brody distribution, with NNSD histograms made of the first 1500 levels. We performed this statistical analysis of the rotational levels and determined the q parameter as a function of the electric field F. Figure 6 shows the evolution of the parameter q for the Brody distribution, for PABN, MABN, and OABN molecules. For $F = 0$, a Poisson distribution ($q = 0$) is obtained for the three isomers, which is the typical behavior for spectra of classically integrable systems. There is an increase in the q value as F increases. At low electric field, the highest values of q are obtained for MABN, while at high electric field, they are observed for OABN. In fact, the evolutions of the q value for MABN and OABN are very similar, with values close to 0.4 at high electric fields. At this value, the amount of chaos is non-negligible (especially for low-lying levels). On the other hand, the evolution of the q value for PABN is much weaker with $q \approx 0.2$ at high electric fields. PABN is a very slightly asymmetric

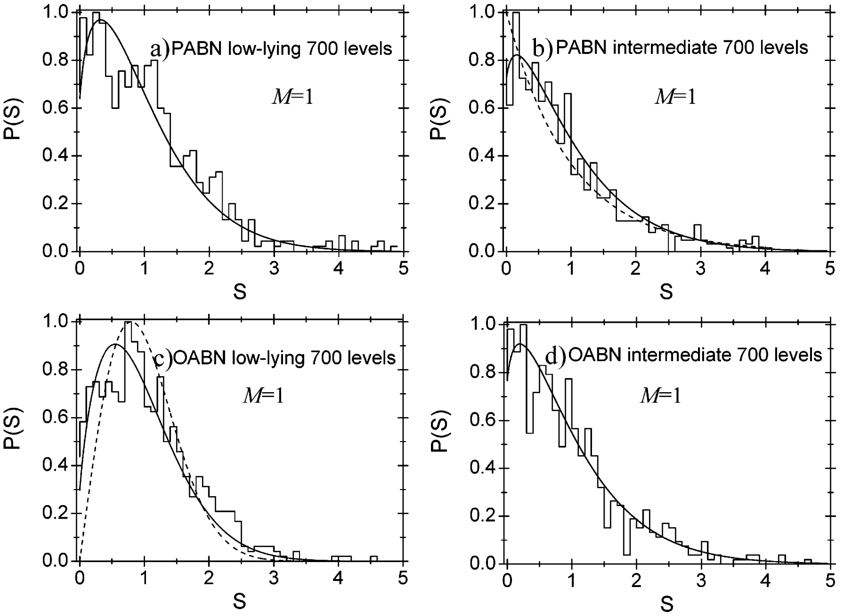

Figure 5. Nearest-neighbor spacing histograms obtained with the procedure described in Appendix A, at $F = 1.21 \times 10^7$ V/m for OABN and PABN. S is the spacing between two adjacent levels. Histograms for the first 700 levels (with $M = 1$) (a) and (c) and for the 701st to the 1400th levels (with $M = 1$) (b) and (d). Dashed curves represent Wigner (c) and Poisson (b) distributions. Full curves are least-squares fits of the histograms by the Brody distribution with the parameter $q = 0.60$ (c), 0.32 (a), 0.21 (d), and 0.17 (b).

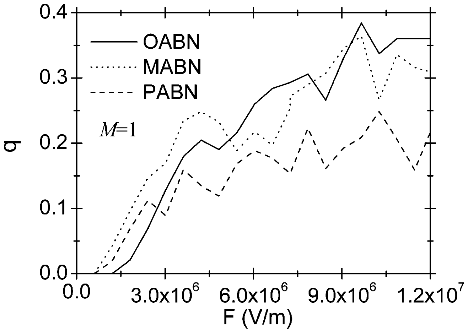

Figure 6. Evolution of the Brody parameter *q* as a function of *F* for OABN (straight line), MABN (dotted line), and PABN (dashed line) for $M = 1$. First 1500 levels were used to determine the Brody parameter.

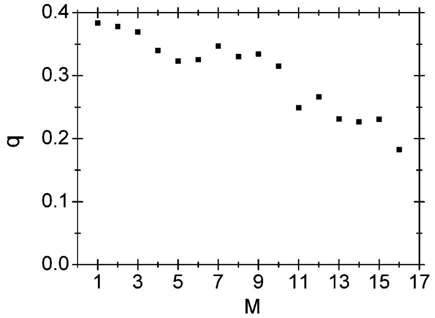

Figure 7. Evolution of the Brody parameter *q* as a function of the quantum state *M* at $F = 1.21 \times 10^7$ V/m for OABN. The first 1500 levels were used to determine the Brody parameter for each value of *M*.

top molecule with dipole moment close to the principal inertia axis (low μ_b, μ_c values) and thus is expected to be, in an electric field, less chaotic than MABN or OABN. This is confirmed by this level of statistical analysis.

One can also study the evolution of this chaotic behavior for ABN isomers in an electric field as a function of the quantum number *M*. Figure 7 presents for OABN, and for $F = 1.21 \times 10^7$ V/m, the evolution of the parameter *q* as a function of *M*. The *q* value slowly decreases from ~0.4 to ~0.2 in the interval $1 \le M \le 15$. This trend is also obtained for MABN and PABN.

To summarize the above discussion, in a static electric field, the rotational motion of an asymmetric molecule is nonintegrable. The chaotic behavior can be quantified by a statistical analysis. The Brody analysis shows that PABN is less chaotic than MABN and OABN. A chaotic motion means that any perturbation on the rotational motion will induce a loss of memory of the initial rotation. Then, the experimental averaged value of μ_z (and the deflection) is different from the one calculated for a rigid rotor. Equation 16 is no longer valid. This explains the difference between experiment and simulation in Figure 2. The next step is to identify a perturbation that prompts a change in trajectories and the modification of the average projection of the dipole moment.

Perturbations to the rotation can be due to vibration−rotation couplings, to inhomogeneities in the electric field, or to interaction with other particles. In fact, interaction between the helium carrier gas and ABN molecules is a sufficient perturbation. In the next paragraph, we describe experiments where we probe this hypothesis by changing the number of collisions between ABN molecules and rare gas atoms in the electric deflector.

6.2. Effect of Collisions on Deflection Profiles. Electric deflection experiments in the presence of a large number of collisions were performed using two experimental methods. The first one consists of introducing a regulated leak of neon in the chamber of the electric deflector. The pressure during normal operation is 2.3×10^{-8} mBar without the neon leak and 3.6×10^{-6} mBar with the neon leak. In the latter case, during the travel through the electric deflector, molecules undergo many long-distance collisions but, at maximum, one frontal collision with neon in the electric deflector. By frontal collisions, we mean collisions with short impact parameter which will induce a significant change in the trajectory and a loss of the molecule. Long-distance collisions are collisions with long impact parameter. They are sufficient for inducing a change of rotational level but without significant modification of the translational trajectory. Thus, the increase in pressure induces an attenuation of the signal and an increase (+25%) in the width of the profile of the beam (without *F*). The second method consists of introducing a constant flow of helium in the source by applying a small constant voltage on the piezo valve. This constant flow increases the effect of the velocity slip between helium and ABN molecules, increasing the number of collisions during the travel of the molecular beam.

Figure 8 shows the variation in the intensity of the signal at the maximum of the peak (I/I_0) as a function of the electric field, for PABN, MABN, and OABN molecules, in the presence of collisions. Clearly, the electric deflection experiments on PABN molecules do not depend on the collision conditions, whereas a strong dependence is observed for MABN and OABN.

In the experiments with the neon leak in the deflector or with the helium leak in the source, the broadening of the beam induced by the electric field is reduced. In this case, there is a clear disagreement between the experiments and the simulation performed for an isolated rigid rotor. For high electric fields ($F > 6 \times 10^6$ V/m), electric deflection profiles are no longer symmetric, and a global deflection of the profile toward high electric field is observed. As an illustration, Figure 9 displays experimental beam profiles of OABN obtained at $F = 0$ V/m and $F = 1.21 \times 10^7$ V/m. These experiments were performed with the constant flow of helium in the source. At $F = 1.21 \times 10^7$ V/m, a weak broadening of the profiles superimposed to a global deflection is observed. The quasi absence of broadening is due to the fact that, with the collisions and the strong chaotic behavior of the rotational trajectories, the molecules have lost the memory of their initial rotational level. They are almost all deflected by the same amount. The loss of memory means that the autocorrelation function of the dipole tends toward zero as the molecules travel through the deflector, $\langle \mu_Z(t = 0)\mu_Z(t)\rangle \to 0$ (for $t \to \infty$). In this limiting case, the average value of the dipole on the axis of the electric field $\langle \mu_z \rangle$ would be the same for all the molecules and would be given by the linear response theory[33]

$$\langle \mu_Z \rangle = \frac{\langle \mu^2 \rangle_{F=0}}{3kT} + \alpha \tag{18}$$

where $\langle \mu^2 \rangle_{F=0}$ is the average value of the square dipole of the molecule calculated at equilibrium without the electric field (at temperature $T = 300$ K) and α is the static electronic polarizability. The deflection obtained using $d = -K_g/mv^2 \langle \mu_Z \rangle F_z\, \partial F_Z/\partial Z$ would be 0.81 mm, with $\alpha = 13.4$ Å^3 (calculated at the HF/6-311++G** level of calculation), and $\langle \mu^2 \rangle_{F=0} = 16.56$ D^2 (see Table 1). This calculated deflection is a little higher than the experimental value measured in Figure 9 (~0.5 mm).

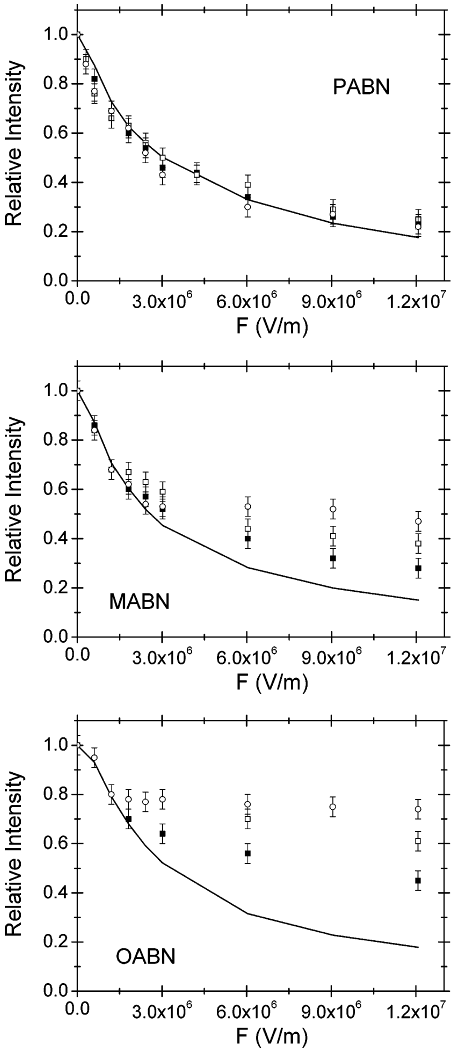

Figure 8. Relative intensity of the beam profile on the beam axis as a function of the electric field F measured with different conditions of collisions. Full squares correspond to experiments with a pressure inside the electric deflector chamber of 2.3×10^{-8} mBar. Open squares correspond to experiments with a neon leak in the electric deflector chamber (3.6×10^{-6} mBar). Open circles correspond to experiments with a small constant flow of carrier helium gas in the molecular beam.

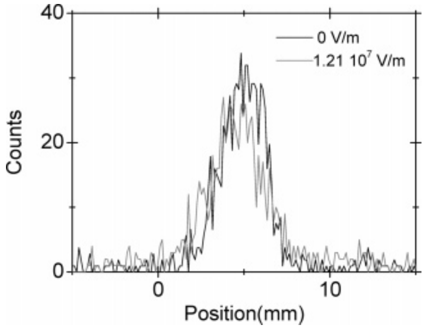

Figure 9. Experimental beam profiles of OABN obtained at $F = 0$ V/m and $F = 1.21 \times 10^7$ V/m. Data were obtained with the constant flow of helium in the source.

Finally, we want to outline that the differences observed in Figure 2 between experiment and simulations are due to collisions between helium atoms and ABN molecules that occur even without the small constant flow. These collisions are due to the velocity distribution and the time width of the pulse of atoms and molecules leaving the source. The differences observed between experiments and simulations can be significantly minimized using a heavier carrier gas. When using neon as carrier gas, the velocity of the beam is reduced (850 m/s instead of 1385 m/s with helium), and the velocity distribution is narrowed. In this case, the narrowing of the velocity distribution diminishes the number of collisions in the deflector. The experimental profiles of deflection are in good agreement with simulations.

7. Conclusion

Electric deflection experiments were performed on the three structural isomers of aminobenzonitrile. Experimental deflection profiles have been compared to calculated profiles obtained using a quantum mechanical treatment of asymmetric molecules in an electric field ($A \neq B \neq C, \mu_a \neq 0, \mu_b \neq 0, \mu_c \neq 0$). Because of the chaotic motion of asymmetric molecules in an electric field and to collisions with other particles, experimental deflection profiles are different from profiles calculated for rigid rotors. The chaotic behavior explains the loss of memory of the initial rotational motion and is a major ingredient to understand the global deflection observed in previous experiments. These results point out the difficulty of measuring a dipole moment by electric deflection of a molecular beam for molecules without symmetry axes and also the difficulty in manipulating such molecules.

In fact, the onset of chaos is determined by a large number of molecular parameters: collisions, the rotational constants, the asymmetry parameter, the magnitude, and the direction of the dipole moment. Some work is in progress in our laboratory to investigate the role of rotation−vibration couplings on the rotation chaotic motion.

Acknowledgment. The authors wish to thank F. Calvo, R. Jost, M. Joyeux, P. Labastie, M. Lombardi, and Vu Ngọc San for helpful discussions. A talk given in a series of lectures organized by the ACI Jeunes Chercheurs, “Analyse Semi-Classique avec Applications Moléculaires” was a starting point to the interpretation of the experimental results.

Appendix A. Statistical Analysis of the Rotational Level Distribution.

A standard statistical analysis of rotation spectra was performed using the method described in refs 32 and 34. First, an unfolding procedure is used to scale the energy-level density, rendering it constant within the whole energy interval, thereby avoiding energy distortions. For the calculated sequence of energy levels E_1^M, E_2^M, ..., E_n^M, we construct the cumulative level density function

$$N(E) = \sum_{i=1}^{n} \Theta(E - E_i^M) \tag{A.1}$$

where $\Theta(E)$ is the Heavyside step function. This function shows a secular variation with energy, which can be approximated by a smooth curve $\tilde{N}(E)$. A polynomial fitting procedure is used to obtain $\tilde{N}(E)$.The spectrum E_i^M is then mapped onto the new spectrum e_i^M through

$$e_i^M = \tilde{N}(E_i^M) \tag{A.2}$$

The new sequence has a constant local mean level density (equal to unity). And the staircase function $n(E) = \sum_{i=1}^{n} \Theta(E - e_i^M)$ fluctuates around the straight line with slope equal to unity.

A widely used statistical measure is the nearest-neighbor spacing distribution (NNSD) $P(S)$. $P(S)$ dS gives the probability of finding pairs of levels (i, $i + 1$) with $e_{i+1}^M - e_i^M$ in the interval $[S, S + dS]$. For a random sequence of energy levels (no interaction between any levels), the NNSD is a Poisson distribution

$$P(S) = \exp(-S) \tag{A.3}$$

In contrast, repulsion between levels leads to a Wigner distribution

$$P(S) = \frac{\pi}{2} S \exp\left(-\frac{\pi S^2}{4}\right) \tag{A.4}$$

This distribution corresponds to a chaotic dynamics for the classical analogue. For intermediate cases, a distribution has been introduced by Brody[34]

$$P(S) = \alpha S^q \exp(-\beta S^{1+q}) \tag{A.5}$$

with $\alpha = (1 + q)\beta$ and $\beta = \Gamma[(2 + q)/(1 + q)]^{(1 + q)}$, where Γ is the gamma Euler function. The statistical parameter q of the Brody distribution is used as a measure of the intensity of the interactions among the levels. q is presented as a measure of the chaotic behavior of a quantum system ($q = 0$ for a Poisson distribution and $q = 1$ for a Wigner distribution).

References and Notes

(1) Special issue on stereodynamics of chemical reactions, and references therein, *J. Phys. Chem. A* **1997**, *101*, 7461.

(2) Brooks, P. R.; Jones, E. M.; Smith, K. *J. Chem. Phys.* **1969**, *51*, 3073.

(3) Kramer, K. H.; Bernstein, R. B. *J. Chem. Phys.* **1964**, *42*, 767.

(4) Parker, D. H.; Bernstein, R. B. *Annu. Rev. Phys. Chem.* **1989**, *40*, 561.

(5) Loesch, H. J.; Remscheid, A. *J. Chem. Phys.* **1990**, *93*, 4779.

(6) Rost, J. M.; Griffin, J. C.; Friedrich, B.; Herschbach, D. R. *Phys. Rev. Lett.* **1992**, *68*, 1299.

(7) Friedrich, B.; Herschbach, D. R. *Nature (London)* **1991**, *353*, 412.

(8) Broyer, M.; Antoine, R.; Benichou, E.; Compagnon, I.; Dugourd, P.; Rayane, D. *C. R. Phys.* **2002**, *3*, 301.

(9) Bonin, K. D.; Kresin, V. V. *Electric-Dipole Polarizabilities of Atoms, Molecules and Clusters*; World Scientific: Singapore, 1997.

(10) Story, T. L., Jr.; Hebert, A. J. *J. Chem. Phys.* **1976**, *64*, 855.

(11) Dugourd, P.; Compagnon, I.; Lépine, F.; Antoine, R.; Rayane, D.; Broyer, M. *Chem. Phys. Lett.* **2001**, *336*, 511.

(12) Compagnon, I.; Hagemeister, F. C.; Antoine, R.; Rayane, D.; Broyer, M.; Dugourd, P.; Hudgins, R. R.; Jarrold, M. F. *J. Am. Chem. Soc.* **2001**, *123*, 8440.

(13) Antoine, R.; Compagnon, I.; Rayane, D.; Broyer, M.; Dugourd, P.; Breaux, G.; Hagemeister, F. C.; Pippen, D.; Hudgins, R. R.; Jarrold, M. F. *J. Am. Chem. Soc.* **2002**, *124*, 6737.

(14) Fraser, G. T.; Pate, B. H. *J. Chem. Phys.* **1993**, *98*, 2477.

(15) Fraser, G. T.; Pate, B. H. *J. Chem. Phys.* **1994**, *100*, 6210.

(16) Farley, F. W.; McClelland, G. M. *Science* **1990**, *247*, 1572.

(17) Farley, F. W.; Novakoski, L. V.; Dubey, M. K.; Nathanson, G. M. *J. Chem. Phys.* **1988**, *88*, 1460.

(18) Rayane, D.; Antoine, R.; Dugourd, P.; Benichou, E.; Allouche, A.-R.; Aubert-Frécon, M.; Broyer, M. *Phys. Rev. Lett.* **2000**, *84*, 1962.

(19) Debye, P. *Polar Molecules*; Dover: New York, 1929.

(20) van Vleck, J. H. V. *Phys. Rev.* **1927**, *30*, 31.

(21) Aquilanti, V.; Bartolomei, M.; Pirani, F.; Cappelletti, D.; Vecchiocattivi, F.; Shimizu, Y.; Kasai, T. *Phys. Chem. Chem. Phys.* **2005**, *7*, 291.

(22) Abd El Rahim, M.; Antoine, R.; Arnaud, L.; Barbaire, M.; Broyer, M.; Clavier, C.; Compagnon, I.; Dugourd, P.; Maurelli, J.; Rayane, D. *Rev. Sci. Instrum.* **2004**, *75*, 5221.

(23) Compagnon, I.; Antoine, R.; Rayane, D.; Broyer, M.; Dugourd, P. *J. Phys. Chem. A* **2003**, *107*, 3036.

(24) Rubio-Pons, O.; Luo, Y. *J. Chem. Phys.* **2004**, *121*, 157.

(25) Frisch, M. J.; Trucks, G. W.; Schlegel, H. B.; Scuseria, G. E.; Robb, M. A.; Cheeseman, J. R.; Zakrzewski, V. G.; Montgomery, J. A., Jr.; Stratmann, R. E.; Burant, J. C.; Dapprich, S.; Millam, J. M.; Daniels, A. D.; Kudin, K. N.; Strain, M. C.; Farkas, O.; Tomasi, J.; Barone, V.; Cossi, M.; Cammi, R.; Mennucci, B.; Pomelli, C.; Adamo, C.; Clifford, S.; Ochterski, J.; Petersson, G. A.; Ayala, P. Y.; Cui, Q.; Morokuma, K.; Malick, D. K.; Rabuck, A. D.; Raghavachari, K.; Foresman, J. B.; Cioslowski, J.; Ortiz, J. V.; Stefanov, B. B.; Liu, G.; Liashenko, A.; Piskorz, P.; Komaromi, I.; Gomperts, R.; Martin, R. L.; Fox, D. J.; Keith, T.; Al-Laham, M. A.; Peng, C. Y.; Nanayakkara, A.; Gonzalez, C.; Challacombe, M.; Gill, P. M. W.; Johnson, B. G.; Chen, W.; Wong, M. W.; Andres, J. L.; Head-Gordon, M.; Replogle, E. S.; Pople, J. A. *Gaussian 98*, revision A.7; Gaussian, Inc.: Pittsburgh, PA, 1998.

(26) Borst, D. R.; Korter, T. M.; Pratt, D. W. *Chem. Phys. Lett.* **2001**, *350*, 485.

(27) Allen, H. C., Jr.; Cross, P. C. *Molecular Vib-Rotors*; John Wiley and Sons, Inc.: New York, 1963.

(28) Townes, C. H.; Schawlow, A. L. *Microwave Spectroscopy*; McGraw-Hill Book Company: New York, 1955.

(29) Since $H_{\mathrm{Stark}} \ll H_{\mathrm{rot}}$, levels that can cross because of the electric field carry essentially the same population. Simulations were also performed assuming a thermal distribution in the deflector, i.e., $p_i^{\mathrm{M}} = \exp[(-E_i^{\mathrm{M}}|_{F_Z})/k_{\mathrm{b}}T]$. The same electric deflection profiles were obtained. For the same reason, diabatic passages (occurring at crossings with very small gaps) are not expected to change the calculated profiles of deflection.

(30) This linear scaling is justified when the rotational constants A, B, and C are small as compared to kT. In this case, the discrete summations over quantum numbers can be replaced by continuous integrations. In the Hamiltonian, the kinetic part is quadratic in angular momenta, and the potential part is linear in electric field F: $H(\sqrt{\alpha}P_\theta, \sqrt{\alpha}P_\varphi, \sqrt{\alpha}P_\psi, \alpha F) = \alpha H(P_\theta, P_\varphi, P_\psi, F)$. The profile of deflection $g(x)$ is given by (see, for example, ref 11)

$$g(x) = \frac{\int\int\int\int\int\int \delta\left(x - K\nabla F \frac{\partial H(P, F)}{\partial F}\right) \exp(-H(P, 0)/kT)\, \mathrm{d}p_\theta\, \mathrm{d}p_\varphi\, \mathrm{d}p_\psi\, \mathrm{d}\theta\, \mathrm{d}\varphi\, \mathrm{d}\psi}{\int\int\int\int\int\int \exp(-H(P, 0)/kT) \mathrm{d}p_\theta \mathrm{d}p_\varphi \mathrm{d}p_\psi \mathrm{d}\theta \mathrm{d}\varphi \mathrm{d}\psi}$$

where δ is the δ-Dirac function. With a change of variables in the integration, it is easy to see that the profile $g(x)$ is the same under the transformation $F^* = \alpha F$, $T^* = \alpha T$ (where $K\nabla F$ is constant).

(31) Grozdanov, T. P.; McCarroll, R. *Z. Phys. D* **1996**, *38*, 45.

(32) Haller, E.; Köppel, H.; Cederbaum, L. S. *Chem. Phys. Lett.* **1983**, *101*, 215.

(33) McQuarrie, D. A. *Statistical Mechanics*; Harper & Row: New York, 1976.

(34) Brody, T. A.; Flores, J.; French, J. B.; Mello, P. A.; Pandey, A.; Wong, S. S. M. *Rev. Mod. Phys.* **1981**, *53*, 385.

(35) Berden, G.; van Rooy, J.; Meerts, W. L.; Zachariasse, K. A. *Chem. Phys. Lett.* **1997**, *278*, 373.